This is a repository copy of *Comparative study of image contrast in scanning electron microscope and helium ion microscope*.

White Rose Research Online URL for this paper:
http://eprints.whiterose.ac.uk/124618/

Version: Accepted Version

Article:

O'Connell, R., Chen, Y., Zhang, H. orcid.org/0000-0002-1188-7810 et al. (5 more authors) (2017) Comparative study of image contrast in scanning electron microscope and helium ion microscope. Journal of Microscopy, 268 (3). pp. 313-320. ISSN 0022-2720

https://doi.org/10.1111/jmi.12660

Reuse
Items deposited in White Rose Research Online are protected by copyright, with all rights reserved unless indicated otherwise. They may be downloaded and/or printed for private study, or other acts as permitted by national copyright laws. The publisher or other rights holders may allow further reproduction and re-use of the full text version. This is indicated by the licence information on the White Rose Research Online record for the item.

Takedown
If you consider content in White Rose Research Online to be in breach of UK law, please notify us by emailing eprints@whiterose.ac.uk including the URL of the record and the reason for the withdrawal request.

eprints@whiterose.ac.uk
https://eprints.whiterose.ac.uk/

Comparative study of image contrast in scanning electron microscope and helium ion microscope

Robert O'Connell[1], Yanhui Chen[1,2], Hongzhou Zhang[1*], Yangbo Zhou[1,3], Daniel Fox[1], Pierce Maguire[1], Jing Jing Wang[1], Cornelia Rodenburg[4]

1. School of Physics and CRANN & AMBER, Trinity College Dublin, Dublin 2, Republic of Ireland

2. Institute of Microstructure and Property of Advanced Materials, Beijing University of Technology, Beijing, 100124, China

3. School of Material Science and Engineering, Nanchang University, Nanchang 330031 , Jiangxi, China

4. Department of Materials Science and Engineering, University of Sheffield, Sir Robert Hadfield Building, Mappin Street, Sheffield S1 3JD, United Kingdom

Corresponding to: Prof. Hongzhou Zhang. Email: hongzhou.zhang@tcd.ie

Keywords: Helium ion microscope, scanning electron microscope, secondary electrons, charging effect, contrast reversal

Summary

Images of Ga^+-implanted amorphous silicon layers in a 110 n-type silicon substrate have been collected by a range of detectors in a scanning electron microscope (SEM) and a helium ion microscope (HIM). The effects of the implantation dose and imaging parameters (beam energy, dwell time, etc.) on the image contrast were investigated. We demonstrate a similar relationship for both the HIM Everhart-Thornley and SEM Inlens detectors between the contrast of the images and the Ga^+ density and imaging parameters. These results also show that dynamic charging effects have a significant impact on the quantification of the HIM and SEM contrast.

Non-Expert:

The helium-ion microscope (HIM) is a recent development in the family of charged-particle microscopes and it operates on similar working principles to those of the conventional scanning

electron microscope (SEM). We investigated the effects of imaging parameters on HIM and SEM images using a Ga+ focused ion beam implanted silicon sample. Our results highlight the similarity and difference between the two microscopes and also show that imaging parameters as well as specimen properties have a significant impact on the quantification of HIM and SEM metrology.

Introduction

The helium-ion microscope (HIM) was introduced as a surface imaging tool and made available to the research community in 2006, aiming to address the challenges of critical dimension measurement in the semiconductor industry (Morgan *et al.*, 2006). To form a helium ion beam, the HIM uses a gas field ionisation source, which is very bright ($\sim 4\times10^{9}$ $A\cdot cm^{-2}\cdot sr^{-1}$) and extremely small (about the size of a single atom) (Hill *et al.*, 2008). This means that the He^{+} beam can be focused into an ultrafine probe (~0.25 nm) while still having a reasonable level of beam current (1fA to 100 pA). HIMs operate on similar working principles to those of SEMs (Notte *et al.*, 2007, Inai *et al.*, 2007, Bell, 2009) . Through scattering with sample atoms, beam particles (i.e. electrons in SEM and He^{+} in HIM) can be stopped and retained in the sample, and some of them can be deflected drastically and exit the sample surface as backscattered particles. The particle-specimen interaction also causes the excitation of electrons which may gain enough energy to escape into the vacuum as secondary electrons (SEs). SEs are labelled SE1 if they are excited directly by the primary beam and SE2 if excited by the backscattered particles (Seiler, 1983). To collect SEs and form images, HIM and SEM are equipped with either an Everhart-Thornley (ET) detector or an annular InLens detector (Griffin, 2011). To collect the backscattered particles, an energy selective backscattered (EsB) detector (Garitagoitia Cid *et al.*, 2016) and a microchannel plate detector (MCP) detector can be used in SEM and HIM respectively. Compared with SEM, the HIM imaging has several advantages, such as a better lateral resolution, a larger depth of field, better surface sensitivity and material contrast, and a unique charging compensation mechanism (Kostinski & Yao, 2011, Hill & Faridur Rahman, 2010, Scipioni *et al.*, 2009). A wide range of samples have been imaged using HIM, such as cancer cells (Bazou *et al.*, 2011), graphene (Zhou *et al.*, 2014, Fox *et al.*, 2013, Zhou *et al.*, 2016), polymers (Pearson *et al.*, 2011, Rodenburg *et al.*, 2010) etc. In terms of semiconductor applications, SE dopant contrast imaging has been demonstrated in a SEM (Chakk & Horvitz, 2006, El-Gomati *et al.*, 2004), particularly by using a

low-voltage scanning electron microscope (Itakura *et al.*, 2010, Sealy *et al.*, 2000). HIM imaging has also been used in efforts to quantify dopant concentration and a direct correlation between dopant concentration and SE intensity has been reported (Jepson *et al.*, 2011, Jepson *et al.*, 2009a, Jepson *et al.*, 2009b).

It is well documented that charging has significant effects on image contrast in SEM and may cause contrast reversal (Gressus *et al.*, 1990). However, the effects of imaging parameters and sample charging on the HIM image contrast have rarely been explored in detail. This is a crucial issue for further development and application of HIM imaging in semiconductor metrology. In this paper, we compare images of Ga-implanted Si samples taken with different HIM and SEM imaging modes and investigate the effects of imaging parameters (beam energy, dwell time, etc.) on the image contrast.

Materials and methods

The samples used for imaging are Ga-implanted silicon prepared via focused ion beam (FIB) irradiation of a 110 n-doped silicon substrate. Using a single-crystal doped substrate allows us to focus on the contrast of the irradiated regions since grain contrast and charging of the substrate are absent. In addition, the surface roughness of the pristine substrate is ~ 0.5 nm, which shows no topographical contrast in SE imaging. The effects of dopant type and crystal orientation of the substrate on SE imaging are not investigated in this work. The implantation was conducted using a Zeiss-Auriga FIB at a beam energy of 30 kV and a beam current of 50 pA. Nine regions ($20 \times 20\ \mu m^2$) of the Si surface were irradiated by the Ga^+ beam for a set length of doping time (from 30s to 270 s), corresponding to a range of implantation doses ($2.34{\times}10^{15} - 2.11{\times}10^{16}$ $\mathrm{ions/cm^2}$). Two batches of samples were prepared using the same set of parameters. An atomic force microscope (AFM, Asylum Research MFP-3D™) was employed to characterise the surface morphology of the implanted regions. The Ga concentration was measured using an energy

dispersive X-ray (EDX) spectrometer in a Carl Zeiss-Ultra Plus SEM with a 20 keV electron beam. Raman spectroscopy was carried out at atmospheric pressure with a Renishaw spectrometer equipped with a 488 nm laser and 2400 lines/mm grating. A 100 × objective lens was used. The laser spot size was ∼1 μm. Acquisition time was fixed at 1s with 10 accumulations.

HIM images of the implanted regions were recorded using a MCP and an ET detector in a Carl Zeiss Orion Plus at 30keV. SEM images used for comparison were collected by using multiple detectors (e.g. the ET detector, the Energy Selective Backscattered (EsB) detector and the In-Lens detector) equipped within a Carl Zeiss-Ultra Plus SEM working at an acceleration voltage ranging from 0.5-5 kV. The sample was cleaned for 10 min using a O_2:Ar (1:3) plasma in a Fischione Instruments 1020 plasma cleaner at a chamber pressure of 5mbar before insertion into the SEM or HIM chamber.

The Stopping and Range of Ions in Matter (SRIM) software package (Ziegler *et al.*, 2010) was used to simulate He^+ and Ga^+ ion interaction with the silicon substrate, to generate output plots for ion range (ion depth of penetration into target materials) and straggle (variance of the ion range within target material). The software also tracks ion implantation and material displacement during imaging with ions. CASINO V2.42 software (Drouin *et al.*, 2007) was used for the simulation of the electron interaction.

Discussion

FIB implantation results in Ga implantation as well as sample sputtering and damage (Stevens-Kalceff & Kruss, 2009). Figure 1(a) is the line profiles of the AFM height images collected from regions of three doses. It shows that surface roughness increases with increasing the doping time. The height and root mean square (RMS) roughness of the implanted regions (extracted from the AFM height map) are depicted in Fig 1(b) as a function of the doping time. The height of the implanted region decreases almost linearly with the doping time. For the largest dose used, the

depth of the pit is ~ 50 nm. The RMS roughness of the implanted regions is close to that of the untreated Si surface (~0.15 nm) at low doses ($\sim 10^{15}\ ions/cm^2$) and increases to 5 nm for the largest dose. Figure 1(c) depicts the dependence of the average intensity of Ga K_α signal in the EDX mapping (the inset image) on the doping time. It is evident that the Ga content in the sample increases linearly with increase in the implantation time, which is consistent with previous reports(Gnaser *et al.*, 2008). The mean projected range of 30kV Ga^+ ions in Si, R_P is 27.8 nm given by the Monte Carlo simulation. Assuming all the ions are retained in the substrate, the peak atomic density of Ga at R_P is $N(\phi_i) = \frac{0.4\phi_i}{\Delta R_p}$, where the straggle, $\Delta R_p = 10.3\ nm$ and ϕ_i is the dose(Nastasi *et al.*, 1996). The Ga atomic density of the 30s-implanted region is $9.09\times 10^{20}\ cm^{-3}$, corresponding to an atomic concentration of 2%. For the highest dose, the Ga concentration is 14%. The Raman spectra of the implanted regions (Fig 1d) indicate that the top-layers of these regions are amorphous (the broad band at 480 cm^{-1}). Si micro-crystallites may exist in these regions, becoming amorphous as the dose increases, since the intensity of the crystalline Si scattering peak (at 521 cm^{-1}) reduces with increasing the Ga^+ dose.

For the HIM and SEM investigation, images of the Ga-implanted amorphous silicon were recorded by using several detectors. The contrast of the implanted region is extracted from the images, which is defined as $C = (I_d - I_s)/I_s$, where I_d is the image intensity obtained from the implanted region, I_s is the intensity from the substrate adjacent to the implanted region. Figure 2(a) shows images of the nine areas using the detectors in SEM and HIM respectively. The contrast is depicted in Fig. 2(b) as a function of the Ga atomic density of the implanted region. For all the implanted regions, HIM-MCP, SEM-EsB and SEM-ET images exhibit positive contrast. This means that the implanted region is brighter than the substrate adjacent to it in these images. The contrast in the SEM-EsB and SEM-ET images is linearly dependent on the Ga atomic density of the implanted region, but the HIM-MCP contrast seems to not vary within experimental uncertainty. The signals

collected by the SEM-EsB and HIM-MCP detectors are mainly back scattered particles. The backscattering coefficient is proportional to Z^2 where Z is the atomic number of the target and it is expected that a heavier Ga target ($Z = 31$) produces more backscattered particles than a lighter Si target ($Z = 14$). For the backscattered electrons (BSEs), our Monte Carlo simulation (see Fig 3) shows that the BSE yield, η_e, increases linearly from 0.26 to 0.30 when the implantation dose increases from $2.34\times10^{15}\ ion/cm^2$ to $2.11\times10^{16}\ \mathrm{ions/cm^2}$. The linear dependence of the SEM-EsB contrast on the Ga density can be attributed to the increase in BSE yield, which is dominated by atomic number contrast. The SEM-ET contrast also carries the material information from the sample and linearly depends on the Ga density since a large portion of the SEM-ET signal is composed of SE2s and excited by backscattered electrons (Fig 3(a)). The two linear relationships have different slopes, which might be due to the variation in the BSE angular distribution and the difference between the collection efficiency of the EsB and ET detector systems.

The HIM-MCP detects backscattered He^+ ions and the backscattered efficiency (Joy & Griffin, 2011) is also proportional to Z^2, which varies by about 10% over the implantation range. The backscattered yield of 30 keV He^+ ions in Si is about 0.012, two orders of magnitude smaller than that of a 5-keV electron beam. Thus, atomic number contrast due to the change in Ga density in the implanted regions is buried in noise due to the low overall backscattered yield. This can explain the insensitivity of the HIM-MCP contrast to the Ga density. We note that the implanted regions are much brighter than the substrate, despite the insensitivity to the Ga density. This may be attributed to the de-channeling of the ions in the top amorphous layer, which increases the backscattered yield of the implanted regions compared with the 110 crystalline Si. Note that very thin surface layers were reported to result in strong contrast due to de-channelling in HIM (Hlawacek *et al.*, 2016)

The SEM-InLens contrast of the implanted region has negative values and decreases monotonically with increasing the Ga atomic density (see Fig. 2(b)). Typical Ga dopant contrast would be expected to result in positive contrast even in SEM-InLens images if the silicon crystallinity was largely preserved as Ga is a p-type dopant. The negative and hence reversed contrast observed here, points again to a strong role of the amorphous surface layer on the contrast. The HIM-ET contrast shows a similar dependence, where the sign of the HIM contrast changes from positive to negative as the Ga density increases (i.e. contrast reversal). Contrast reversal has been observed in SEM-InLens imaging of insulators by varying electron beam energies (Le Gressus *et al.*, 1990, Dapor *et al.*, 2009). The similarity between HIM-ET and SEM-InLens imaging indicates that they share the same contrast mechanism. It has been shown that the dominant SEM-InLens signal is the SE1 component which is excited directly by the primary beam (Griffin, 2011). In the HIM, the low He^+ backscattering efficiency results in negligible SE2 contribution to the HIM-ET imaging and the dominant signal for the HIM-ET detector is also SE1.

To understand the contrast reversal, we first investigate the effects of beam energy on the SEM-InLens images. Figure 4 (a) shows the images collected through a range of beam energies (0.5- 5 keV) and at a fixed dwell time per pixel of 4.32 μs. The contrast is depicted as a function of the beam energy in Fig. 4(b). The contrast decreases and reaches negative values as the beam energy E_p increases and contrast reversal occurs for all the implanted regions. However, the contrast reversal appears at a lower E_p for the implanted regions with a higher Ga density. The difference between the contrast of the implanted regions appears to be more significant as the beam energy increases. The contrast also varies with the dwell time. Figure 5 (a) is composed of the images collected with a fixed beam energy of 0.5 keV and a dwell time in the range of 0.54-4.32 μs, and the corresponding contrast is shown in Fig. 5(b) as a function of the dwell time. It is evident that the contrast increases with increasing dwell time. For the most heavily implanted regions (Ga density $> 2.7{\times}10^{21}\ cm^{-3}$), contrast reversal occurs because of changing the dwell time. As

shown in Fig. 5 (c) and (d), the dwell time has similar effects on the HIM-ET imaging. The HIM-ET contrast also increases with increasing dwell time and contrast reversal is observed for the implanted regions with a Ga density $> 9\times10^{20}\ cm^{-3}$.

It is known that SEM contrast changes with imaging conditions and sample charging has been proposed for the mechanism of contrast reversal (Cazaux, 2004, Cazaux, 2008). To understand the SEM-InLens contrast observed in our experiment, we sketch the dependence of SE yield on the beam energy, i.e. $\delta(E_p)$ in Fig. 6(a). The amorphous region has a smaller work function than that of the crystalline silicon (Ukah *et al.*, 1988) and hence a larger peak SE yield compared with the Si substrate. The mean free path of SEs also varies with the Ga density, and the SE escape depth varies accordingly. In terms of $\delta(E_p)$, we speculate the amorphous region behaves more like an insulator (Seiler, 1983), which means $\delta(E_p)$ has a narrower peak and shifted towards lower beam energy as the Ga density increases. When the implanted region has the same SE yield as the substrate, the contrast of the region is 0. We assume the SE yield is δ_{Si}, δ_h and δ_l for the substrate and the regions with a high and low Ga density respectively, and the beam energy is E_h when $\delta_{Si} = \delta_h$. We define E_l in a similar way, e.g. E_l is defined as the primary beam energy at which $\delta_{Si} = \delta_l$. When the beam energy, E_p is lower than E_h, the contrast of the implanted region is positive since $\delta_h > \delta_{Si}$. When $E_h < E_p < E_l$, the contrast of the high-Ga region becomes negative and contrast reversal happens. When the beam energy increases to a value larger than E_l (at which $\delta_l = \delta_{Si}$), all the implanted regions exhibit negative contrast. Figure 6(a) also explains the decrease of the contrast in the beam energy observed in Fig. 4(b) since the ratio of $\delta_{h,l}/\delta_{Si}$ decreases as the beam energy increases.

The charging effects may play the key role in the dwell-time effects shown in Fig. 5(a) and (b). The amorphous Ga-implanted regions have limited electrical conductivity and thus charge accumulation occurs when irradiated by a charged-particle beam. For a 0.5 keV electron beam, the

electron range is smaller than the thickness of the amorphous layer (see Fig. 3(a)). Therefore, the charging behaviour of the Ga implanted region is solely determined by the properties of the top amorphous layer, irrelevant to the underlying Si substrate. As shown in Fig. 6(b), if the beam energy E_p is in the range of $E_h < E_p < E_l$, $\delta_h < \delta_{Si} < \delta_l < 1$ and the high-Ga and low-Ga regions have a negative and positive contrast respectively. For the high-Ga region, the landing energy of the primary beam reduces as negative charges build up in the region ($\delta_h < 1$). For a coarse approximation, we treat the region as an ideal insulator and the charging stops when the SE yield becomes unity (the red arrow in Fig.6(b)). A larger dwell time results in more negative charges accumulated in the surface layer, lowering the landing energy of the electron beam. Consequently, a beam of lower landing energy produces a larger δ_h. The contrast reversal occurs when $\delta_h > \delta_{Si}$. For the low-Ga region, δ_l increases but $\delta_l > \delta_{Si}$ during the charge process and the contrast of the low-Ga region is positive which increases with increasing dwell time. We note that the presence of a native oxide layer of varying thickness usually covers silicon surfaces. This may cause nonuniform charging of the substrate and the grey levels are hence not constant across the substrate. The typical thickness of the native oxide is < 1 nm (Morita *et al.*, 1990), which is much smaller than the 0.5-keV beam range. Therefore, the variation in δ_{Si} due to charging may not be as significant as the implanted regions.

However, the $\delta(E_p)$-related charging effects cannot directly be applied to the HIM-ET contrast reversal shown in Fig. 5 (c) and (d) where the contrast increases with increasing dwell time. This is because the SE yield in HIM is much larger than unity (Ishitani *et al.*, 2010) and the charging effects would cause a continuous decrease in contrast when the dwell time increases and the SE yield of the implanted regions decreases towards unity. As shown in Fig. 3(b), most of the He^+ ions penetrate the top insulating implanted layer and the charging of the top layer is mainly due to the emission of SEs. The positive charges built in the layer reduces the SE emission and are responsible for the observed negative contrast. As the dwell time increases, the amount of the

positive charges will reduce due to diffusion to the underneath Si substrate and thus the contrast increases, i.e. the implanted region appears less dark and the magnitude of the contrast decreases. The charge diffusion is more significant for the low-Ga region because it has a lower degree of damage induced by the Ga implantation. This may be responsible for the positive HIM contrast of the lowest-Ga region and the contrast reversal for the region next to it in Fig. 5(c). Hence the HIM-ET contrast reversal is a good indicator of limited charge mobility due to implantation damage. To avoid distortions of the implantation profile due to charging long dwell times are recommended.

Conclusion

Amorphous Ga-implanted Si regions were prepared on a Si substrate by using Ga^+ FIB irradiation. The Ga atomic density in each 30-nm-thick implanted region varies from $9.1\times 10^{20}\ cm^{-3}$ to $8.1\times 10^{21}\ cm^{-3}$. Images of the regions were collected by using the InLens, ET, EsB detectors in a SEM as well as MCP and ET detectors in a HIM. The SEM-EsB and ET images show materials contrast which linearly depends on the Ga density and is attributed to the Z-dependence of the backscattered electron yield. The HIM-MCP images do not show material contrast due to the low yield of backscattered ions, but the visibility of the implanted regions in the images may be due to the de-channeling effects of the top amorphous layer. HIM-ET and SEM-InLens images bear the most similarity and the dominant signal of the two types of imaging is SE1. In both cases, the contrast decreases linearly with increasing Ga density and for each implanted region the contrast increases with dwell time. The modification of the SE yield due to the Ga implantation as well as the dynamic charging effect are responsible for the dependence of the SEM-InLens contrast on the imaging parameters, while charge diffusion may be the key factor that causes the observed contrast reversal in the HIM ET images. This work may be beneficial to further development of quantitative SEM and HIM imaging for semiconductor metrology and analysis.

Acknowledgements

The work at the School of Physics and the Centre for Research on Adaptive Nanostructures and Nanodevices at Trinity College Dublin is supported by Science Foundation Ireland [grant No: 11/PI/1105, 07/SK/I1220a and 08/CE/I1432] and the Irish Research Council [grant No: GOIPG/2014/972 and EPSPG/2011/239]. The project was supported by the Royal Society through international exchanges grant IE140211 and The Leverhulme Trust for the PicoFib network. CR thanks EPSRC for funding under EP/N008065/1.

Reference

Bazou, D., Behan, G., Reid, C., Boland, J. J. & Zhang, H. Z. (2011) **Imaging of human colon cancer cells using He-Ion scanning microscopy**. *Journal of Microscopy,* **242,** 290-294.

Bell, D. C. (2009) Contrast Mechanisms and Image Formation in Helium Ion Microscopy. *Microscopy and Microanalysis,* **15,** 147-153.

Cazaux, J. (2004) Charging in scanning electron microscopy "from inside and outside". *Scanning,* **26,** 181-203.

Cazaux, J. (2008) On some contrast reversals in SEM: Application to metal/insulator systems. *Ultramicroscopy,* **108,** 1645-1652.

Chakk, Y. & Horvitz, D. (2006) Contribution of dynamic charging effects into dopant contrast mechanisms in silicon. *J Mater Sci,* **41,** 4554-4560.

Dapor, M., Jepson, M. A. E., Inkson, B. J. & Rodenburg, C. (2009) The Effect of Oxide Overlayers on Secondary Electron Dopant Mapping. *Microscopy and Microanalysis,* **15,** 237-243.

Drouin, D., Couture, A. R., Joly, D., Tastet, X., Aimez, V. & Gauvin, R. (2007) CASINO V2.42—A Fast and Easy-to-use Modeling Tool for Scanning Electron Microscopy and Microanalysis Users. *Scanning,* **29,** 92-101.

El-Gomati, M. M., Wells, T. C. R., Müllerová, I., Frank, L. & Jayakody, H. (2004) Why is it That Differently Doped Regions in Semiconductors are Visible in Low Voltage SEM? *IEEE TRANSACTIONS ON ELECTRON DEVICES,* **51**.

Fox, D., Zhou, Y. B., O'Neill, A., Kumar, S., Wang, J. J., Coleman, J. N., Duesberg, G. S., Donegan, J. F. & Zhang, H. Z. (2013) **Helium ion microscopy of graphene: beam damage, image quality and edge contrast**. *Nanotechnology,* **24**.

Garitagoitia Cid, A., Rosenkranz, R. & Zschech, E. (2016) Optimization of the SEM Working Conditions: EsB Detector at Low Voltage. *Advanced Engineering Materials,* **18,** 185-193.

Gnaser, H., Brodyanski, A. & Reuscher, B. (2008) Focused ion beam implantation of Ga in Si and Ge: fluence-dependent retention and surface morphology. *Surface and Interface Analysis,* **40,** 1415-1422.

Gressus, C. L., Valin, F., Gauthier, M., Duraud, J. P., Cazaux, J. & Okuzumi, H. (1990) Charging phenomena on insulating materials: Mechanisms and applications. . *Scanning,* **12,** 203-210.

Griffin, B. J. (2011) A Comparison of Conventional Everhart-Thornley Style and In-Lens Secondary Electron Detectors-A Further Variable in Scanning Electron Microscopy. *Scanning,* **33,** 162-173.

Hill, R. & Faridur Rahman, F. H. M. (2010) Advances in helium ion microscopy. *Nuclear Instruments and Methods in Physics Research Section A: Accelerators, Spectrometers, Detectors and Associated Equipment,* **645,** 96-101.

Hill, R., Notte, J. & Ward, B. (2008) The ALIS He ion source and its application to high resolution microscopy. *Physics Procedia,* **1,** 135-141.

Hlawacek, G., Jankowski, M., Wormeester, H., van Gastel, R., Zandvliet, H. J. W. & Poelsema, B. (2016) Visualization of steps and surface reconstructions in Helium Ion Microscopy with atomic precision. *Ultramicroscopy,* **162,** 17-24.

Inai, K., Ohya, K. & Ishitani, T. (2007) Simulation study on image contrast and spatial resolution in helium ion microscope. *Journal of Electron Microscopy,* **56,** 163-169.

Ishitani, T., Yamanaka, T., Inai, K. & Ohya, K. (2010) Secondary electron emission in scanning Ga ion, He ion and electron microscopes. *Vacuum,* **84,** 1018-1024.

Itakura, M., Kuwano, N., Sato, K. & Tachibana, S. (2010) Variations in contrast of scanning electron microscope images for microstructure analysis of Si-based semiconductor materials. *Journal of Electron Microscopy,* **59(Supplement),** S165-S173.

Jepson, M., Liu, X., Bell, D., Ferranti, D., Inkson, B. & Rodenburg, C. (2011) Resolution Limits of Secondary Electron Dopant Contrast in Helium Ion and Scanning Electron Microscopy. *Microscopy and Microanalysis,* **17,** 637-642.

Jepson, M. A. E., Inkson, B. J., Liu, X., Scipioni, L. & Rodenburg, C. (2009a) Quantitative dopant contrast in the helium ion microscope. *Epl,* **86,** 5.

Jepson, M. A. E., Inkson, B. J., Rodenburg, C. & Bell, D. C. (2009b) Dopant contrast in the helium ion microscope. *Epl,* **85,** 4.

Joy, D. C. & Griffin, B. J. (2011) Is Microanalysis Possible in the Helium Ion Microscope?

. *Microsc. Microanal.,* **17,** 643-649.

Kostinski, S. & Yao, N. (2011) Rutherford backscattering oscillation in scanning helium-ion microscopy. *Journal of Applied Physics,* **109,** 064311.

Le Gressus, C., Valin, F., Gautier, M., Duraud, J. P., Cazaux, J. & Okuzumi, H. (1990) Charging phenomena on insulating materials: Mechanisms and applications. *Scanning,* **12,** 203-210.

Morgan, J., Notte, J. & Raymond Hill, B. W. (2006) An Introduction to the Helium Ion Microscope. *Microscopy today,* **14,** 24-31.

Morita, M., Ohmi, T., Hasegawa, E., Kawakami, M. & Ohwada, M. (1990) Growth of native oxide on a silicon surface. *Journal of Applied Physics,* **68,** 1272-1281.

Nastasi, M., Mayer, J. & Hirvonen, J. K. (1996) *Ion-Solid Interactions,* Cambridge University Press.

Notte, J., Ward, B., Economou, N., Hill, R., Percival, R., Farkas, L. & McVey, S. (2007) An introduction to the helium ion microscope. In: *Frontiers of Characterization and*

Metrology for Nanoelectronics: 2007 (eds. D. G. Seiler, A. C. Diebold, R. McDonald, C. M. Garner, D. Herr, R. P. Khosla & E. M. Secula). Amer Inst Physics, Melville.

Pearson, A. J., Boden, S. A., Bagnall, D. M., Lidzey, D. G. & Rodenburg, C. (2011) Imaging the Bulk Nanoscale Morphology of Organic Solar Cell Blends Using Helium Ion Microscopy. *Nano Letters,* **11,** 4275-4281.

Rodenburg, C., Liu, X., Jepson, M. A. E., Zhou, Z., Rainforth, W. M. & Rodenburg, J. M. (2010) The role of helium ion microscopy in the characterisation of complex three-dimensional nanostructures. *Ultramicroscopy,* **110,** 1178-1184.

Scipioni, L., Sanford, C. A., Notte, J., Thompson, B. & McVey, S. (2009) Understanding imaging modes in the helium ion microscope. *Journal of Vacuum Science & Technology B,* **27,** 3250-3255.

Sealy, C. P., Castell, M. R. & Wilshaw, P. R. (2000) Mechanism for secondary electron dopant contrast in the SEM. *Journal of Electron Microscopy* **49,** 311-321.

Seiler, H. (1983) SECONDARY-ELECTRON EMISSION IN THE SCANNING ELECTRON-MICROSCOPE. *Journal of Applied Physics,* **54,** R1-R18.

Stevens-Kalceff, M. A. & Kruss, D. P. (2009) Focused ion beam induced local modifications of the contact potential difference of n- and p-doped silicon. *J. Phys. D: Appl. Phys. ,* **42** 145117 (145117pp).

Ukah, C. I., Kruzelecky, R. V., Racansky, D., Zukotynski, S. & Perez, J. M. (1988) In situ work function measurements in evaporated amorphous silicon. *Journal of Non-Crystalline Solids,* **103,** 131-136.

Zhou, Y., Fox, D. S., Maguire, P., O'Connell, R., Masters, R., Rodenburg, C., Wu, H., Dapor, M., Chen, Y. & Zhang, H. (2016) **Quantitative secondary electron imaging for work function extraction at atomic level and layer identification of graphene**. *Scientific Reports,* **6,** 21045.

Zhou, Y., O'Connell, R., Maguire, P. & Zhang, H. (2014) **High throughput secondary electron imaging of organic residues on a graphene surface**. *Scientific Reports,* **4,** 7032.

Ziegler, J. F., Ziegler, M. D. & Biersack, J. P. (2010) SRIM - The stopping and range of ions in matter (2010). *Nuclear Instruments and Methods in Physics Research Section B: Beam Interactions with Materials and Atoms,* **268,** 1818-1823.

Figure Captions

FIG. 1. The effects of doping time on morphology of the FIB-implanted Si (a) representative AFM traces of the height profiles (b) the AFM height and RMS roughness as a function of implantation time (c) the average intensity of the EDX Ga signal (K_{α}) extracted from the EDX Ga mapping (inset image) and (d) Raman spectra of the FIB-implanted Si

FIG. 2. (a) Images of the doping contrast using different detectors (acquisition time: 4-5 μs) and (b) the relationship between theoretical doping concentration and image contrast. For SEM imaging, the beam energy is 5 keV, dwell time 4.32 μs, working distance 5 mm, field of view $140 \mu m \times 180 \mu m$. For HIM imaging, the beam energy is 30 keV, dwell time 1 μs, working distance 5 mm, field of view $125 \mu m \times 125 \mu m$.

FIG 3. Monte Carlo simulation of the electron (a) and ion (b) trajectories respectively in the implanted region (the thickness of the top implanted layer is 30nm and the trajectories in red in (a) represents BSEs) (c) BSE yield of a 5 keV electron beam as a function of the implanted Ga atomic density calculated by the simulation.

FIG. 4. (a) SEM-InLens images of the implanted regions collected under different beam energies (0.5-5 keV) and a dwell time of 4.32 μs. (b) The SEM-InLens contrast as a function of the beam energy for three implanted regions.

FIG. 5. (a) SEM-InLens images taken with different dwell times (in μs) and a fixed beam energy of 0.5 keV. (b) The SEM-InLens contrast as a function of the dwell time. (c) HIM-ET images taken with different dwell times (in μs) and a fixed beam energy of 35 keV. (b) The HIM-ET contrast as a function of the dwell time.

FIG. 6. (a) The SE yield as a function of the primary electron beam: E_h and E_l are the two beam energies where $\delta_h = \delta_{Si}$ and $\delta_l = \delta_{Si}$ respectively. (b) The charging effects in the

implanted regions: The landing energy of the electron beam decreases as the dwell time increases when $\delta < 1$ for an insulator sample.

Figure1.

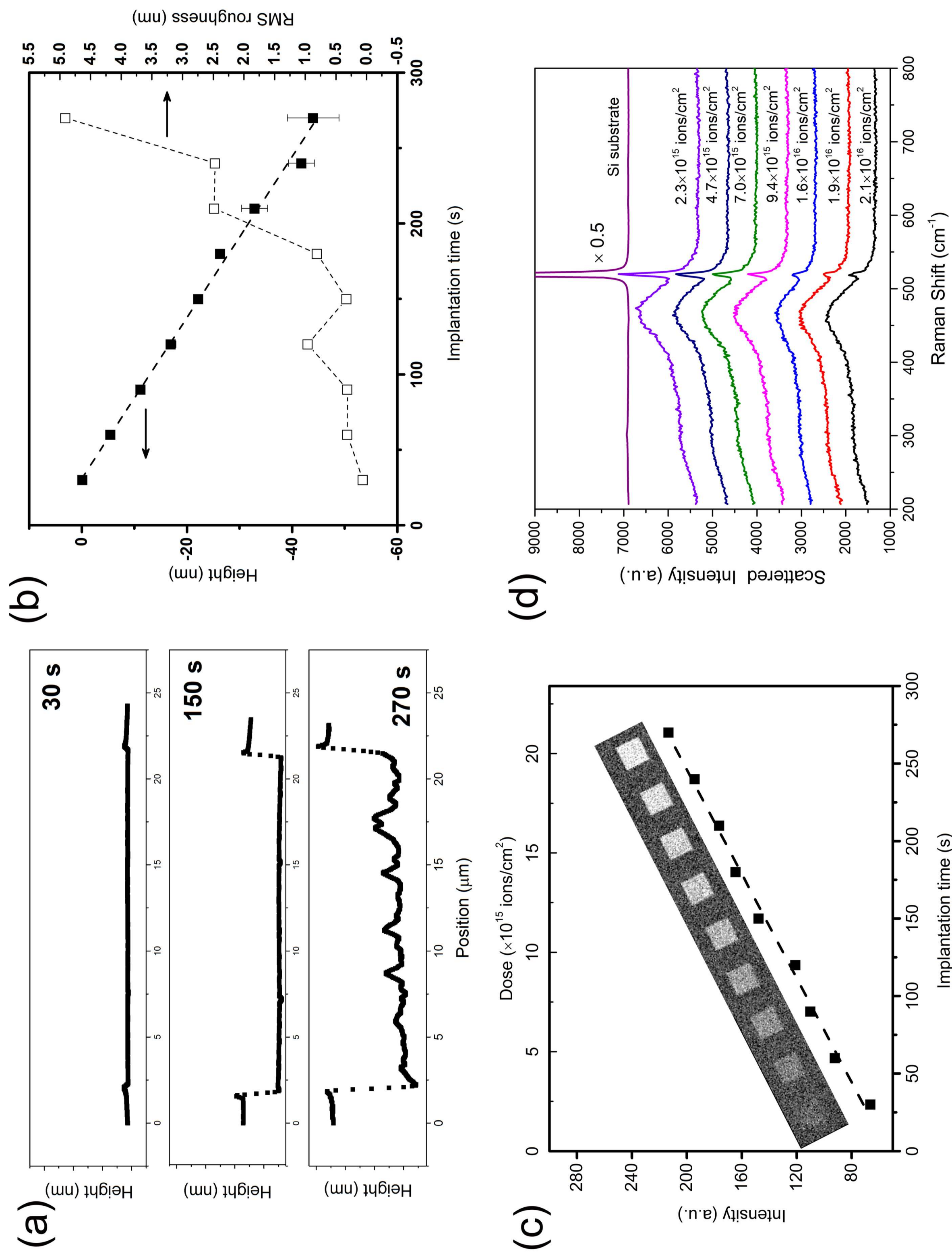

Figure 2.

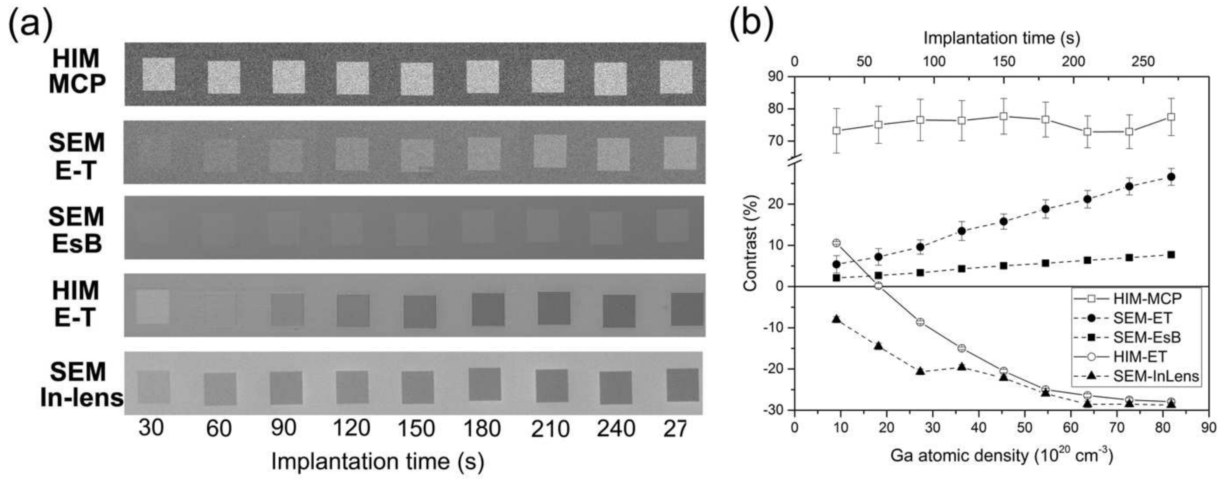

Figure 3.

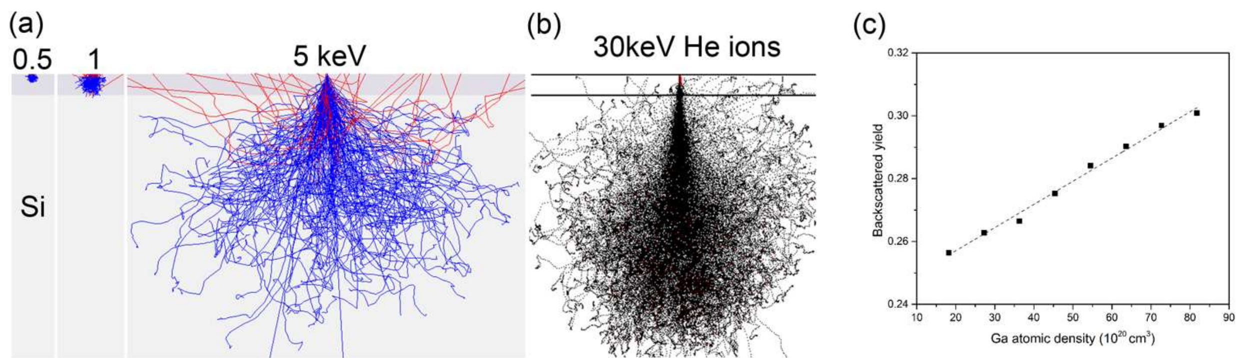

Figure 4.

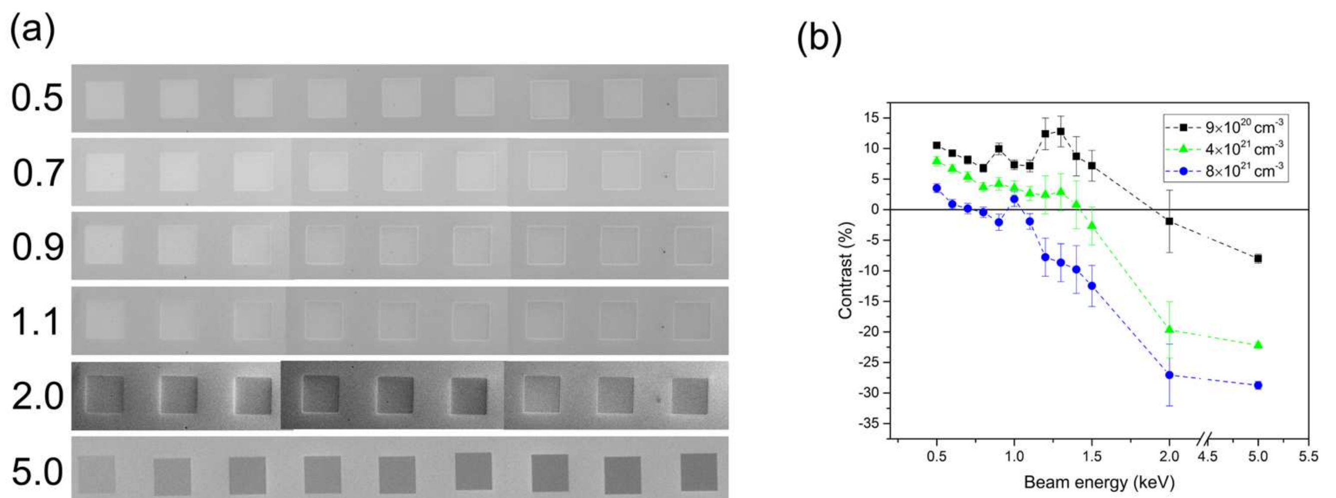

Figure 5.

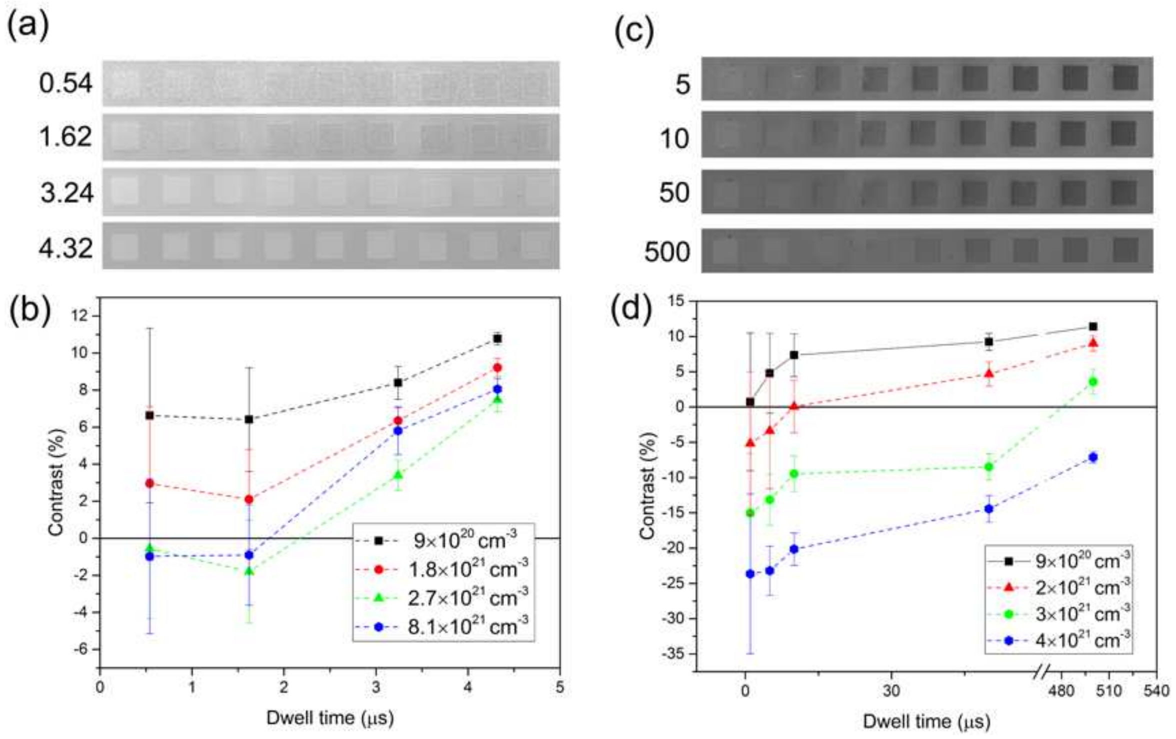

Figure 6.